

Visualizing the Radial and Circumferential Strain Distribution Within Vessel Phantoms Using Synthetic-Aperture Ultrasound Elastography

Sanghamithra Korukonda, *Student Member, IEEE*, and Marvin M. Doyley, *Member, IEEE*

Abstract—Noninvasive elastography (NIVE) produces elastograms that are difficult to interpret because NIVE visualizes strain in the transducer coordinate system. In this paper, we hypothesized that transforming normal and shear strain elastograms to the vessel coordinate system will produce better strain elastograms. To corroborate this hypothesis, we acquired synthetic-aperture (SA) ultrasound data from simulated and physical vessel phantoms. In both studies, SA echo frames were reconstructed from data acquired with a sparse transducer array. The simulation study was performed with homogeneous and heterogeneous phantoms, but in the experimental study we used a modified ultrasound scanner to acquire SA data from homogeneous ($n = 1$) and heterogeneous ($n = 3$) vessel phantoms. Axial and lateral displacements were estimated by performing two-dimensional cross-correlation analysis on the beamformed RF echo frames. We generated radial and circumferential strain elastograms by transforming normal and shear strain elastograms to the vessel coordinate system. The results revealed: 1) radial and circumferential strain elastograms acquired from simulated data had a relative root mean squared error on the order of 0.1%; 2) experimentally acquired radial and circumferential strain elastograms had elastographic contrast-to-noise ratio (CNRe) between 10 and 40 dB, and elastographic signal-to-noise ratio (SNRe) between 10 and 35 dB, depending on the number of active transmission elements employed during imaging; 3) radial and circumferential strain elastograms produced with fewer than 8 active transmission elements were inferior to those computed with a greater number of active elements; and 4) plaques were evident in the strain elastograms, except in those obtained with the sparsest transducer array. This study demonstrated that a synthetic-aperture ultrasound system could visualize radial and circumferential strain noninvasively.

I. INTRODUCTION

STROKE causes many deaths and disabilities in the Western world [1]; it can occur after a life-threatening plaque ruptures in the carotid artery [2]. Techniques such as vascular angiography, multi-slice computed tomography (CT) and high-resolution magnetic resonance imaging (MRI) can visualize the carotid artery [3], but they are unsuitable for mass screening. For example, vascular angiography can assess the extent of stenosis, but the extent of

stenosis is a poor indicator of cerebrovascular event—composition, not stenosis, is the key determinant of plaque to rupture [4]. Multi-slice CT can visualize the carotid atherosclerosis [5], but like angiography, it cannot characterize plaque composition. High-resolution MRI can characterize plaque compositions [6], but MRI is expensive and inflexible, traits that make it an inappropriate screening tool. Ultrasound (US) is relatively inexpensive and more flexible than MRI. Furthermore, ultrasound can assess the extent of stenosis and characterize plaque burden [7]–[9], but it cannot characterize plaque composition [10].

Cardiologists may use noninvasive vascular elastography (NIVE) to identify patients who are predisposed to developing life-threatening plaques. Noninvasive vascular elastography visualizes the carotid artery's strain distribution [11], a mechanical parameter that can characterize different plaque types [10]. However, NIVE images are difficult to interpret because strain is measured in the transducer coordinate system (Cartesian) rather than the vessel's coordinate system (polar), as illustrated in Fig. 1. We hypothesized that transforming the measured strain from Cartesian to polar coordinates will overcome this limitation, provided accurate estimates of both axial and lateral components of displacements are available. Researchers have measured the axial and lateral components of displacement with two-dimensional echo tracking [12] and optical-flow-based displacement estimation techniques [13]. Both techniques have produced reliable axial displacement estimates, but the quality of the lateral displacement estimates is limited. Consequently, transforming axial and lateral strain from the transducer coordinate system to the vessel coordinate system has not produced useful radial or circumferential strain elastograms.

Researchers have developed alternate approaches to measuring radial strain but most are unable to visualize circumferential strain. For example, acceptable radial strain elastograms have been produced by performing NIVE on longitudinal sections of the carotid artery [14]–[16], because in this scan plane, the axial and radial strains are similar. However, the low precision of lateral-displacement estimates prevents this scanning method from producing useful longitudinal strain elastograms. Rather than visualizing radial strain, Maurice *et al.* [11] visualized the Von Mises parameter—a mechanical parameter that is independent of the coordinate system. Although the Von Mises parameter is a suitable surrogate for radial strain,

Manuscript received November 10, 2011; accepted April 30, 2012. This work was supported by startup funds from the University of Rochester.

The authors are with the Hajim School of Engineering and Applied Sciences, Department of Electrical and Computer Engineering, University of Rochester, Rochester NY (e-mail: m.doyley@rochester.edu).

DOI <http://dx.doi.org/10.1109/TUFFC.2012.2370>

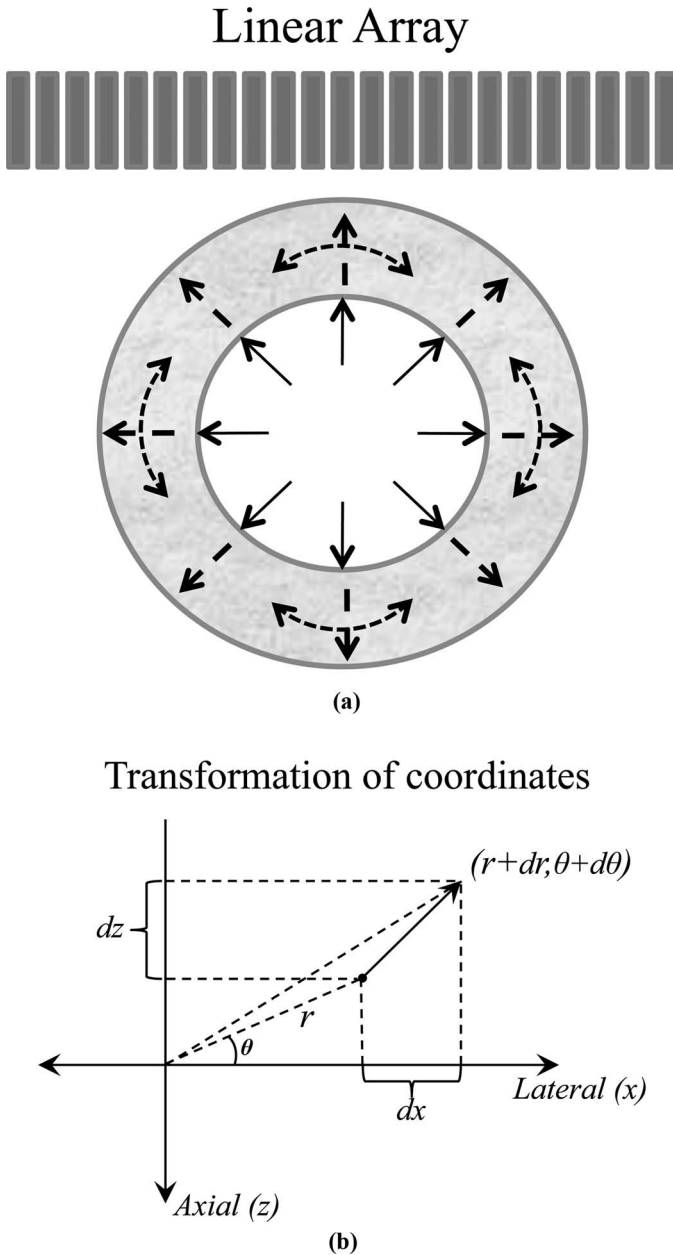


Fig. 1. (a) Schematic diagram showing a carotid artery undergoing non-invasive elastographic imaging; (b) system used to transform axial and lateral coordinates (z, x) to radial and circumferential directions (r, θ) .

it does not provide any information about circumferential strain. Hansen *et al.* [17] initially developed an angular compounding method that produced encouraging radial and circumferential strain elastograms.

Here we present another approach for producing high-precision axial and lateral strain elastograms. The precision of displacement estimates depends on the extent of the point-spread function (PSF). More specifically, the narrower the PSF is, the more precise are the displacement estimates. Most displacement estimators can supply precise axial displacements, because in the axial direction the PSF is narrow. However, the relatively broad lateral PSF prevents most displacement estimators from supplying precise lateral displacement estimates [18]. Beamform-

ing methods have been used to reduce the effective width of the lateral PSF [19]–[22]. Besides reducing the width of the lateral PSF, Konofagou and Ophir [23] demonstrated that increasing the lateral sampling frequency of RF echo frames by a sufficiently large factor will also reduce the variance incurred when measuring lateral displacements. We have recently developed a prototype of a synthetic-aperture (SA) ultrasound elastographic imaging system that produces RF echo frames with sufficiently high lateral sampling frequency and narrow beam widths to produce high-precision lateral displacement estimates [24]. Because it is difficult to produce SA imaging systems with high frame rates, we have demonstrated that this limitation may be overcome by using a sparse transducer array [25]–[27].

This paper reports the results of simulated and phantom studies that were conducted to determine the feasibility of developing noninvasive vascular elastography based on SA ultrasound imaging. We made two assumptions in this study: 1) SA ultrasound elastography systems can estimate axial and lateral displacements with high precision, and 2) transforming the measured axial and lateral displacements to the vessel coordinate system would produce acceptable radial and circumferential strain elastograms. We corroborated these assumptions by conducting experiments on simulated and physical vessel phantoms. In both studies, we measured the motion (axial and lateral components of displacement) incurred in the phantoms by applying a 2-D cross-correlation echo tracking method to RF echo frames acquired with a 5-MHz transducer array when operating with 128, 32, 8, and 2 active transmission elements. We used a finite-difference strain estimator to compute normal and shear strain elastograms from the measured axial and lateral displacement estimates. Radial and circumferential strain elastograms were computed by applying a coordinate transformation procedure to the normal and shear strain elastograms. Three performance metrics were used to assess the quality of the resulting radial and circumferential strain elastograms: the root mean squared error (RMSE), the elastographic signal-to-noise ratio (SNRe), and the elastographic contrast-to-noise ratio (CNRe).

II. MATERIALS AND METHODS

A. Simulation Study

The finite element method (FEM), together with the Field II acoustic model [28], was used to predict the displacement of RF echo patterns when the carotid artery was imaged under different physiological conditions. The RF echo frames were used to demonstrate the feasibility of developing a NIVE system based on synthetic-aperture ultrasound imaging. In the proceeding subsections, we describe the two key stages of the simulation tool: mechanical and acoustic modeling.

TABLE I. PHYSICAL PROPERTIES OF THE L14-5/38 LINEAR TRANSDUCER ARRAY.

Number of elements	128
Center frequency	7.5 MHz
Frequency bandwidth	65%
Elevation height	4.0 mm
Element width	0.2789 mm
Element pitch	0.3048 mm
Kerf	0.025 mm
Elevational focus	16.0 mm

1) *Mechanical Model*: Finite element representations of a healthy carotid and a diseased artery were created with Abacus/CAE (Dassault Systèmes, Vélizy-Villacoublay, France), a commercially available finite-element package. Both arteries had inner and outer diameters of 1.5 and 6 mm, respectively. All elements in the healthy artery were assigned Young's modulus of 40 kPa, and Poisson's ratio of 0.495. These mechanical parameters were chosen to represent those reported in [17]. The diseased vessel model contained a soft crescent-shaped plaque. We assigned Young's moduli of 25 and 50 kPa to the elements in the plaque and artery wall, respectively. Both tissue types were assumed to be nearly incompressible (i.e., a Poisson's ratio of 0.495 was assigned to all regions). In both models, we simulated a pressure difference of 666.61 Pa by applying a uniformly distributed pressure to the inner lumen, which generated an applied strain of $\approx 1\%$. This represents the pressure difference between a pair of RF echo frames and not the absolute pressure within the vessel. The nodes on the outer boundary were constrained from moving in the radial and circumferential directions.

2) *Acoustic Model*: We used the acoustic field simulation program, Field II [28] to simulate the synthetic aperture response of a commercially available L14-5/38 linear array (Prosonic Corporation, Seoul, Korea) that was operating at 5 MHz, the maximum frequency that could be used with this array for SA imaging. The transducer parameters are summarized in Table I. To simulate the acoustic response of the pre-deformed artery, we randomly distributed a sufficient number of point scatterers (16 scatterers per wavelength) within the simulated vessel to generate fully developed speckles [29]. To simulate the acoustic response of the post-deformed vessel, we used the displacement fields computed using the FEM to redistribute the point scatterers. The speed of sound and attenuation coefficient of the simulated vessel were assumed to be

1540 m/s and 0.5 dB/MHz/cm, respectively. We synthesized echo data with an SNR of 20 dB by adding Gaussian-distributed white noise to the synthetic aperture data. Five groups of noisy RF echo frames were reconstructed from SA data acquired with 128, 32, 8, and 2 active transmission elements.

B. Experimental Study

We performed phantom studies to evaluate the performance of a synthetic aperture-based NIVE system under controlled experimental conditions. The goal of these studies was to determine how the prototype system of NIVE performed with homogeneous and heterogeneous vessel phantoms with elasticity contrasts of -2 , -1.5 , and 2.0 .

1) *Phantom Fabrication*: We fabricated four vessel phantoms, each 20 mm outer diameter \times 15 cm long, from bovine skin gelatin (Type B, Bloom 200, Gelatin Innovation Inc., Chicago, IL); agar (Difco Reagents, BD Diagnostic Systems, Sparks, MD); corn starch (Wegmans, Rochester, NY); and degassed de-ionized water (18M Ω). We used a Landmark Servo-Hydraulic Test System (MTS, Eden Prairie, MN) that was equipped with a 5-N load cell to measure the mechanical properties of representative cylindrical samples (20 mm diameter by 20 mm height) of all phantoms components.

We fabricated an elastically homogeneous vessel phantom by pouring molten gel (15% by weight gelatin, 1% by weight agar, and 2% by weight corn starch) into a cylindrical mold (20 mm diameter \times 15 cm long) that had a central cylindrical rod (3 mm diameter). We sealed the phantom and stored it at 4°C for approximately 24 h to ensure that the mechanical properties were stabilized before imaging, as recommended by [30].

The procedure used to fabricate the heterogeneous phantoms that contained eccentric plaques can be summarized into four steps: 1) fabricate the vessel wall by pouring the molten gel into a cylindrical mold that has an off-centered cylindrical rod (6 mm diameter) inside; 2) cool the vessel to 4°C in a refrigerator for 1 h; 3) remove the cylindrical rod, and replace it with a 3-mm-diameter rod; 4) fill the vacant cavity between the vessel wall and the rod with a different gel suspension, and allow the resulting phantom to set for 24 h at 4°C. Table II gives the composition of the materials used to fabricate each phantom.

TABLE II. COMPOSITION IN PERCENTAGE BY WEIGHT (%W) OF MATERIAL USED TO FABRICATE VESSEL PHANTOMS.

Phantom type	Gelatin (%w)	Agar (%w)	Water (%w)	Cornstarch (%w)	Measured E (kPa)	Elasticity contrast
Vessel wall	15.0	1	82.0	4	81.3 ± 4.1	
Plaque #1	18.4	1	74.6	6	139.5 ± 1.4	+1.92
Plaque #2	10.6	1	82.4	6	57.2 ± 0.2	-1.52
Plaque #3	8.7	1	84.3	6	36.1 ± 0.3	-2.15

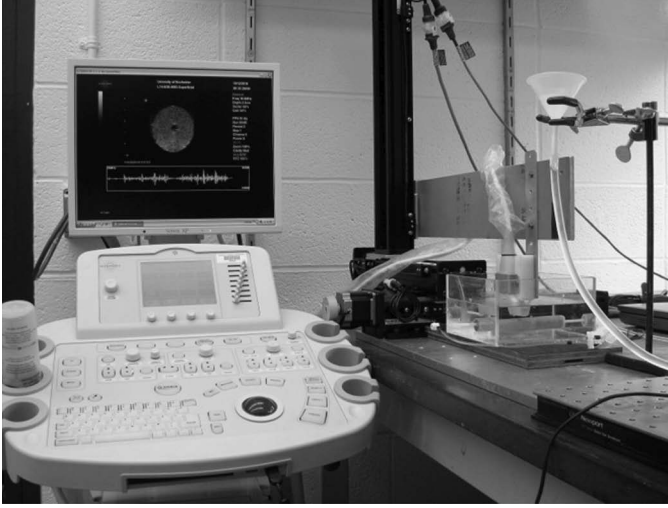


Fig. 2. Experimental setup showing the suspended vessel phantom being imaged by an L14-5/38 linear array probe attached to a SonixRP ultrasound scanner.

2) *Data Acquisition*: All echo imaging was performed with a commercial Sonix RP ultrasound scanner (Ultrasonix Corp., Richmond, BC, Canada) as shown in Fig. 2. This scanner was equipped with a 128-element linear transducer array (L14-5/38 probe), and was configured to operate with a transmission frequency of 5 MHz, and a sampling frequency of 40 MHz. The scanner was programmed using the software development kit (TEXO SDK, v10.7, Ultrasonix Medical Corp., Vancouver, BC, Canada), to fire each element in the linear array sequentially, and to receive on all 128 elements. We performed all imaging in water tank of $15 \times 15 \times 10$ cm, which was filled with degassed water. A simple water column system was used to pressurize the vessels (from 100 mmHg) in steps of 5 mmHg, which was measured with a pressure gauge (Model Omega DPG1000ADA, Omega Engineering Inc., CT). All experiments were repeated five times, to assess the repeatability of our measurement process.

C. Image Reconstruction

We used the sum-delay technique to reconstruct synthetic aperture images. More specifically, we reconstructed the signal, S , at any given point in the image as

$$s(P) = \sum_{i=1}^N \sum_{j=1}^N w_{ij} T_{ij}(t - \tau_P), \quad (1)$$

where $T_{ij}(t)$ represents the RF echo generated when the i th element transmits and the j th element receives; t represents the time of flight of the echo. The round-trip time from point P , the number of elements in the array, and the apodization weights are denoted by τ_P , N , and w_{ij} , respectively. Unlike fully-SA imaging, in which all of the elements in the aperture are active during transmission and reception, in sparse array imaging, only a few elements in the array are active during transmission. We used a

transmit-receive (T/R) matrix, similar to those shown in Fig. 3, to compute apodization values that produced a beam pattern similar to that generated with a fully populated array [27], [31]. The rows and columns of the T/R matrix represent the transmitting and receiving elements, respectively; and the coefficients represent the corresponding apodization weights. Fig. 3(a) shows an example of the T/R matrix for a fully SA array ($N = 5$)—every element is used to both transmit and receive ultrasound signals, and thus has a unit value. Projecting the cross-diagonal of the T/R matrix produces a triangular function of length $2N - 1$. Fig. 3(b) shows the corresponding T/R matrix for a sparse array in which alternate elements in the T/R matrix are active during transmission. The matrix coefficient of the inactive elements is zero, and the coefficients of the active elements are adjusted to produce a triangular function. Four sets of RF echo frames were reconstructed from each data set, to simulate the cases in which data were acquired with 128, 32, 8, and 2 active transmit elements that spanned the full length of the array. All RF echo frames were reconstructed with a lateral sampling frequency of 52 lines/mm and beam width of 0.2 mm at the center of the phantom.

D. Displacement and Strain Estimation

We estimated the axial and lateral displacements by applying the 2-D echo tracking technique described in [32] to the pre-and post-deformed RF echo frames. All echo tracking was performed with 0.8×0.8 mm kernels that overlapped by 75% in both coordinate directions. Sub-pixel displacements were estimated by fitting a 2-D parabolic function to the top of the cross-correlation function. A 5×5 median filter was applied to the axial and lateral displacement elastograms (dz and dx respectively), to eliminate spurious displacement estimates. We computed the normal ($\varepsilon_{zz}, \varepsilon_{xx}$) and shear components of strain (γ_{zx}, γ_{xz}) by applying a finite difference operator (∇) to the axial and lateral displacement elastograms:

$$\begin{bmatrix} \varepsilon_{zz} & \gamma_{xz} \\ \gamma_{zx} & \varepsilon_{xx} \end{bmatrix} = \nabla \begin{bmatrix} dz & dx \end{bmatrix}. \quad (2)$$

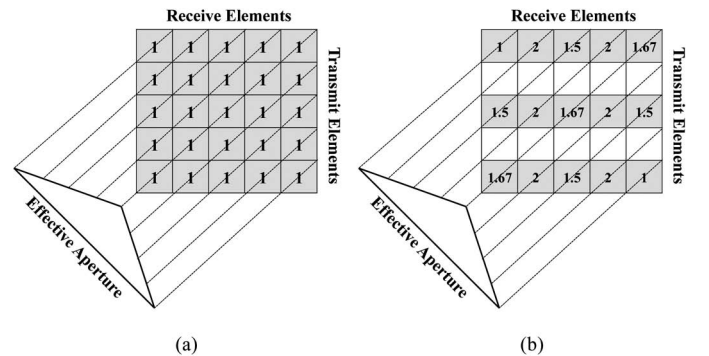


Fig. 3. Sample transmit-receive matrices for (a) a fully populated array (all transducer elements were active), and (b) a sparse array (alternate transducer elements were active).

To facilitate coordinate transformation, we estimated the center of the vessel lumen (C_x, C_z) by fitting an ellipse to the lumen boundary in a least-squares sense. Once the center of the vessel was estimated, we computed radial and circumferential strain elastograms by transforming the normal and shear strains to the polar vessel coordinate system (r, θ) as

$$\{\varepsilon'\} = T_\varepsilon \{\varepsilon\}, \quad (3)$$

where $\varepsilon = [\varepsilon_{xx} \ \gamma_{xz} \ \gamma_{zx} \ \varepsilon_{zz}]^T$ is the strain tensor in the transducer coordinate system, $\{\varepsilon'\} = [\varepsilon_r \ \gamma_{r\theta} \ \gamma_{\theta r} \ \varepsilon_\theta]^T$ is the strain tensor in the vessel coordinate system, and T_ε is the transformation matrix. ε_{rr} and $\varepsilon_{\theta\theta}$ represent the radial and circumferential strains, respectively; whereas $\gamma_{r\theta}$ and $\gamma_{\theta r}$ represent the shear strains in polar coordinates. The transformation matrix T_ε is given by [33]

$$T_\varepsilon = \frac{1}{x^2 + z^2} \begin{bmatrix} x^2 & xz & xz & z^2 \\ -xz & x^2 & -z^2 & xz \\ -xz & -z^2 & x^2 & xz \\ z^2 & -xz & -xz & x^2 \end{bmatrix}. \quad (4)$$

The radial (ε_{rr}) and circumferential ($\varepsilon_{\theta\theta}$) strains elastograms were computed from (3) and (4) as

$$\varepsilon_{rr} = \frac{1}{x^2 + z^2} [x^2 \varepsilon_{xx} + xz(\gamma_{xz} + \gamma_{zx}) + z^2 \varepsilon_{zz}] \quad (5)$$

$$\varepsilon_{\theta\theta} = \frac{1}{x^2 + z^2} [z^2 \varepsilon_{xx} - xz(\gamma_{xz} + \gamma_{zx}) + x^2 \varepsilon_{zz}]. \quad (6)$$

E. Data Analysis

The quality of the elastograms was assessed qualitatively by visual inspection, and quantitatively using three performance metrics: RMSE, SNRe, and CNRe. The RMSE performance metric was used only in the simulation study, and was defined as

$$\text{RMSE} = \sqrt{[(\hat{\theta} - \theta)^2]}, \quad (7)$$

where θ and $\hat{\theta}$ represent the true and estimated elastogram (strain or displacement), respectively.

The SNRe was used to assess the quality of simulated and experimental elastograms obtained from the homogeneous vessel phantoms, and was defined as

$$\text{SNRe(dB)} = 20 \log \left[\frac{\varepsilon_w}{\sigma_w^2} \right], \quad (8)$$

where ε_w represents the mean radial and circumferential strain, and σ_w^2 represents the variance in the estimated strain.

The CNRe performance metric was used to assess the performance of elastograms obtained from the heterogeneous phantoms. In elastography, CNRe is defined as [34]

$$\text{CNRe(dB)} = 20 \log \left[\frac{2(\varepsilon_w - \varepsilon_p)^2}{(\sigma_w^2 + \sigma_p^2)} \right], \quad (9)$$

where ε_w and ε_p represent the mean strain values in the wall and plaque, respectively; σ_w and σ_p represent the standard deviation in strain values in the vessel wall and plaque, respectively. Because the strains generated in vessels are not stationary, CNRe represents a relative measure of contrast-to-noise ratio.

III. RESULTS

We evaluated the performance of radial and circumferential strain elastograms produced with four different sparse arrays. These studies were conducted with synthetic aperture data that were acquired from simulated and physical vessel phantoms. The results are presented in the form of images, strain profiles, and tables.

A. Simulation Study

1) *Homogeneous Vessel*: Fig. 4 shows theoretical strain elastograms computed using the FEM. Axial and lateral displacement elastograms were symmetric about the vertical and horizontal axes of the vessel, respectively [Figs. 4(a) and 4(b)]. Axial and lateral strains had a rosette pattern of areas of alternating low and high strains [Figs. 4(c) and 4(d)]. The radial and circumferential strain elastograms were circularly symmetric [Figs. 4(e) and 4(f)], attaining their peak value on the inner lumen, with values that decreased rapidly with increasing radial distance. This strain decay was consistent with that predicted using analytical methods [35], [11].

Fig. 5 shows strain elastograms (axial and lateral; radial and circumferential) computed from SA data that was acquired with 128, 32, 8, and 2 active transmission elements. The strain elastograms were similar to those computed using the FEM, but elastograms computed from SA data obtained with fewer than eight active transmission elements produced elastograms that were corrupted with artifacts. Fig. 6 shows the corresponding radial and circumferential strain profiles computed from the strain elastograms shown in Figs. 5(c) and 5(d). The mean strain profiles agreed well with theory, irrespective of sparsity (i.e., the number of active transmission elements); but the variance incurred was dependent on sparsity. Table III reports the errors incurred by the homogeneous elastograms obtained with different levels of sparsity. The most accurate strain elastograms were produced from SA data acquired with more than eight active transmission elements. The accuracy of circumferential strain elastograms were comparable to the radial strain elastograms, which was expected because radial and circumferential strains were reconstructed from axial, lateral, and shear strains using (5) and (6).

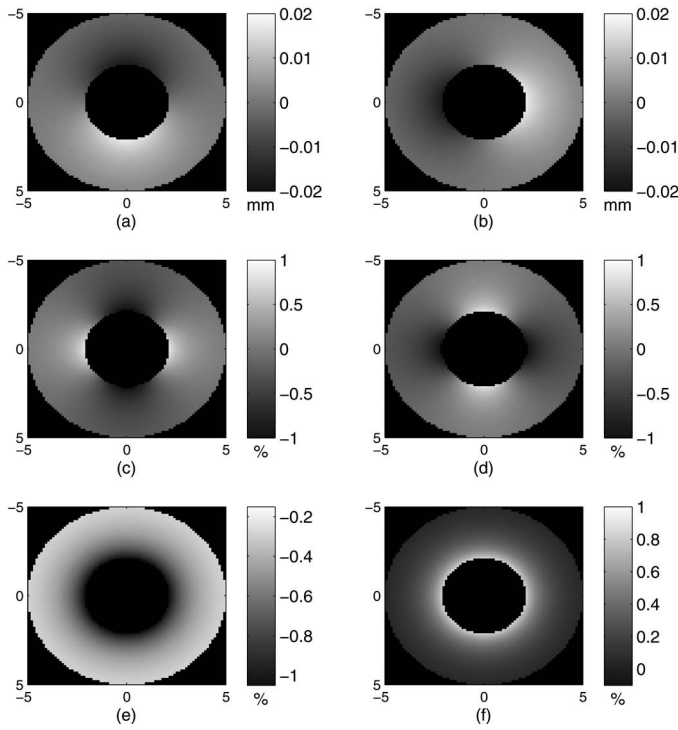


Fig. 4. The spatial variation of displacement and strain within a homogeneous vessel, which was computed using the finite element method. (a) and (b) axial and lateral displacements, (c) and (d) axial and lateral strain, and (e) and (f) radial and circumferential strain.

SNRe of both radial and circumferential elastograms increased rapidly with an increasing number of active transmission elements, but plateaued after 32 active transmission elements (Fig. 7).

Fig. 8 shows the vertical and horizontal transects through the PSFs obtained with 128, 32, 8, and 2 active transmission elements. The vertical transects were similar [Fig. 8(a)], which was expected, because the transmission and pulse repetition frequencies of all transducer arrays were identical. The horizontal transects [Fig. 8(b)] of the PSFs produced with 32 or more active transmission elements were indistinguishable, with a narrow main lobe and negligible side lobes. The main lobe of horizontal transects were similar except for the one obtained using two active transmission elements. Side lobes were visible in sparse arrays with fewer than eight active transmission elements.

2) *Heterogeneous Vessel*: Figs. 9(a) and 9(b) show theoretical axial and lateral displacements computed using the FEM. Figs. 9(c) and 9(d) show the axial and lateral strains. The corresponding radial and circumferential strain elastograms are shown in Figs. 9(e) and 9(f).

Fig. 10 strain elastograms estimated from SA data that was acquired with 128, 32, 8, and 2 active transmission elements. Increasing sparsity degraded the quality of both displacement and strain elastograms. Radial and circum-

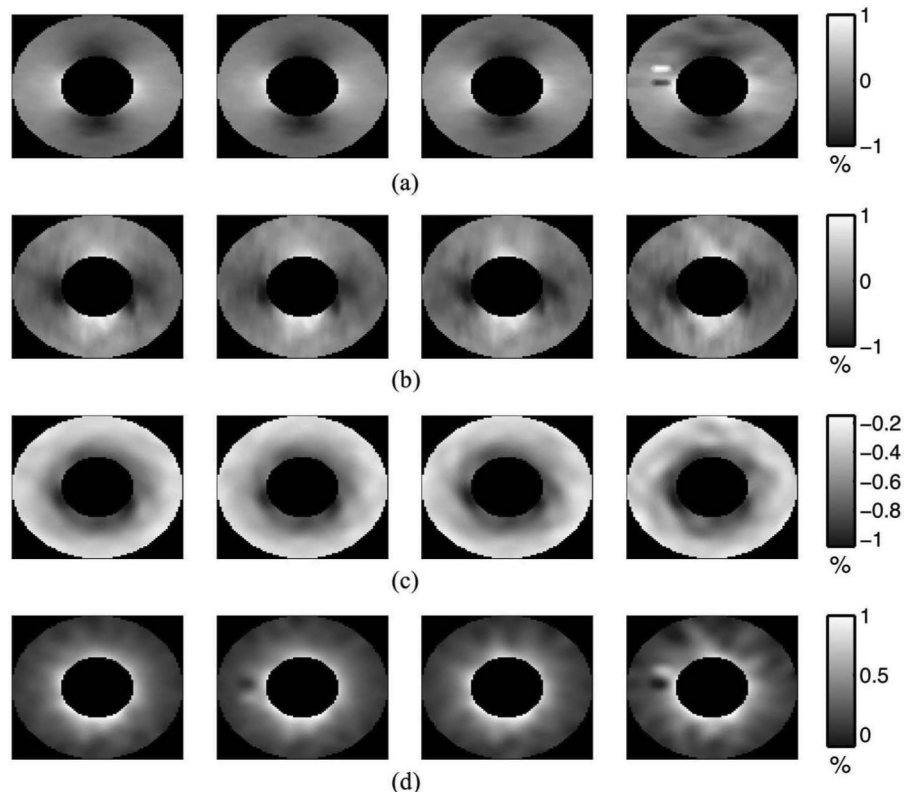


Fig. 5. Homogeneous elastograms computed from simulated RF echo frames for transducer arrays with (left to right) 128, 32, 8, and 2 active transmission elements. (a) Axial and (b) lateral strain elastograms. (c) Radial and (d) circumferential strain elastograms. The marked annulus denotes the area over which the elastographic signal-to-noise ratio values reported in Fig. 7 were computed.

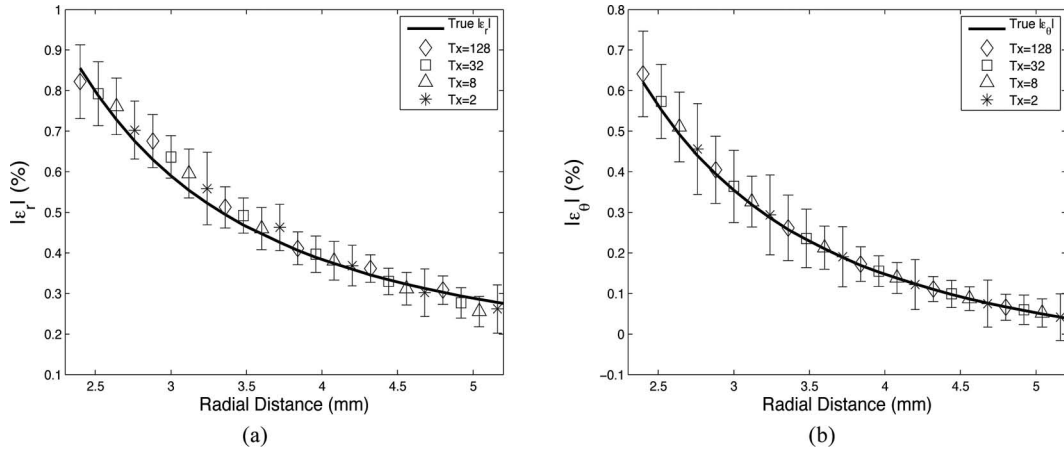


Fig. 6. (a) Radial and (b) circumferential strain profiles computed from the homogeneous strain elastograms shown in Figs. 5(c) and 5(d).

ferential strain elastograms (Fig. 10) revealed the plaque, but radial strain elastograms provided better contrast. The eccentric lumen did not affect image quality because all elastograms were computed in the vessel's coordinate system.

Fig. 11 shows the CNRe, computed from the radial and circumferential strain elastograms shown in Figs. 10(c) and 10(d), plotted as a function of sparsity. In both cases, reducing sparsity increased CNRe. The results suggest that sparse array with as few as eight active transmission elements can produce useful elastograms. Table IV reports the errors incurred by the heterogeneous elastograms obtained at different levels of sparsity.

B. Experimental Study

We performed experimental studies to corroborate the simulation study, and to evaluate the performance of the prototype of our synthetic-aperture ultrasound elastographic system under controlled experimental conditions. We used four phantoms in this investigation—a homogeneous vessel phantom, and soft plaque phantoms with

elasticity contrasts of -2 , -1.5 , and 2 , respectively. Fig. 12 shows representative examples of sonograms obtained from the homogeneous and heterogeneous phantoms using fully populated SA ultrasound imaging.

Fig. 13 shows representative examples of radial and circumferential strain elastograms obtained from the homogeneous vessel phantom. These elastograms were computed from SA echo frames obtained with 128, 32, 8, and 2 active transmission elements. Radial and circumferential strain attained their peak value on the inner lumen, with values that decreased with increasing radial distance, which was consistent with predictions of the simulation study. They also contained artifacts, but evidently circumferential strain elastograms contained more.

Fig. 14 shows the corresponding radial and circumferential strain profiles obtained from Fig. 13. Changing the number of active transmission elements did not influence the mean radial and circumferential strain, but it affected the variance, as predicted by the simulation study. The variance incurred in circumferential strain elastograms was larger than that incurred in the radial elastograms.

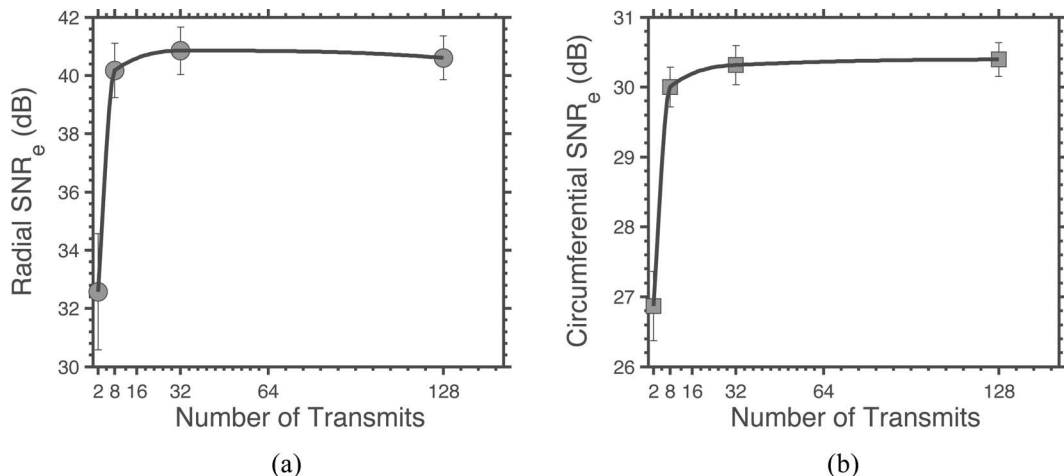


Fig. 7. Elastographic signal-to-noise ratio (SNRe) plotted as function of number of active transmission elements, showing the SNRe computed from (a) radial and (b) circumferential strain elastograms shown in Fig. 6.

TABLE III. THE ROOT MEAN SQUARE ERRORS (RMSEs) COMPUTED FROM HOMOGENEOUS DISPLACEMENT [AXIAL (DZ) AND LATERAL (DX)] AND STRAIN ELASTOGRAMS [RADIAL (ε_{RR}) AND CIRCUMFERENTIAL ($\varepsilon_{\theta\theta}$)] OBTAINED WITH VARYING NUMBER OF ACTIVE TRANSMISSION ELEMENTS (Tx).

Tx	128	32	8	2
dz (μm)	0.435 ± 0.014	0.437 ± 0.053	0.497 ± 0.055	0.677 ± 0.091
dx (μm)	0.576 ± 0.088	0.584 ± 0.161	0.568 ± 0.110	0.786 ± 0.203
ε_{rr} (%)	0.089 ± 0.004	0.091 ± 0.002	0.097 ± 0.002	0.109 ± 0.003
$\varepsilon_{\theta\theta}$ (%)	0.054 ± 0.002	0.055 ± 0.002	0.057 ± 0.002	0.076 ± 0.028

Fig. 15 shows the SNRe computed from the radial and circumferential strain elastograms shown in Fig. 13 plotted as a function of the number of active transmission elements.

Fig. 16 shows a montage of radial and circumferential strain elastograms obtained from three plaque phantoms. Plaques were only discernible in radial elastograms computed from SA that were acquired with more than 8 active transmission elements.

Fig. 17 shows a plot of the CNRe as a function of the number of active transmission elements and elasticity contrast. CNRe increased with increasing number of active transmission elements and elasticity contrast.

IV. DISCUSSION

Noninvasive vascular elastography produces elastograms that are more difficult to interpret than those produced with other approaches to vascular elastography [36], [37], an issue which has hampered its clinical use. Besides improving visual interpretation, an ultrasound elastographic imaging system that measures radial or circumferential strain accurately would allow clinicians to predict the propensity of an atherosclerotic plaque to rupture. More specifically, circumferential stress—a major determinant of atherosclerotic plaque rupture [38] could be computed by applying a suitable model-based inversion technique to radial and circumferential strain elastograms.

This study investigates whether transforming normal and shear strain elastograms, obtained with an SA ultrasound elastographic system, to the vessel coordinate system would provide useful radial and circumferential strain elastograms. The primary findings of this investigation can be summarized as follows:

- 1) Sparse arrays produced high-precision axial and lateral strain elastograms with as few as eight active transmission elements [Figs. 5(a), 5(b), 10(a), and 10(b)].
- 2) The mean radial and circumferential strains were independent of the number of active transmission elements, but the variance incurred when estimating strain was not (Figs. 6 and 14).
- 3) Radial and circumferential strain elastograms obtained from the vessel phantoms agreed with theoretical predictions, but circumferential strain elastograms were inferior (Figs. 5 and 13).
- 4) Plaques were visible in all radial strain elastograms, except those obtained with the sparsest transducer array; however, plaques were poorly visualized in the experimental circumferential strain elastograms (Figs. 13 and 16).
- 5) Increasing the modulus contrast increased the CNRe, but the decrease in performance observed with increasing sparsity was independent of modulus contrast (Fig. 17).

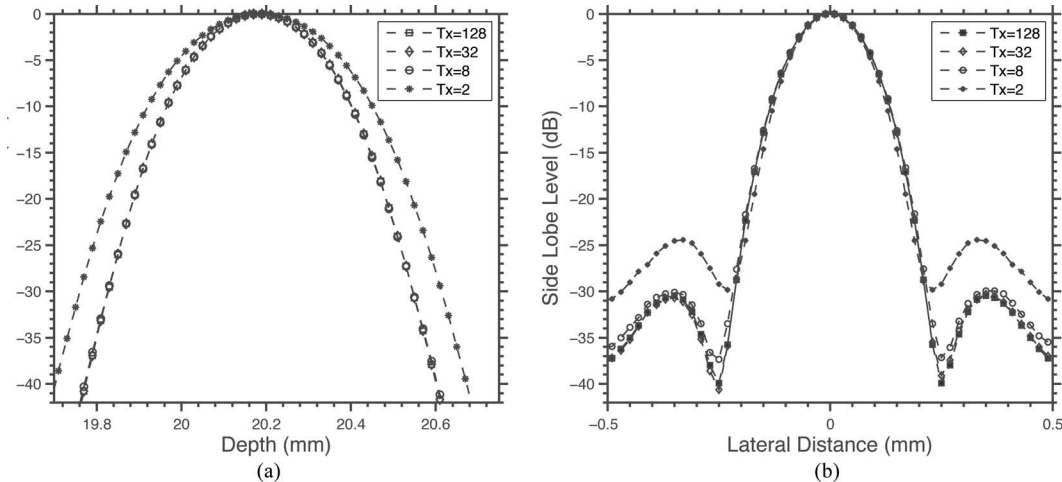


Fig. 8. (a) Vertical and (b) horizontal profiles of the point-spread function obtained from a scatterer located at a depth of 20 mm when reconstruction was performed with 128, 32, 8, and 2 active transmission elements.

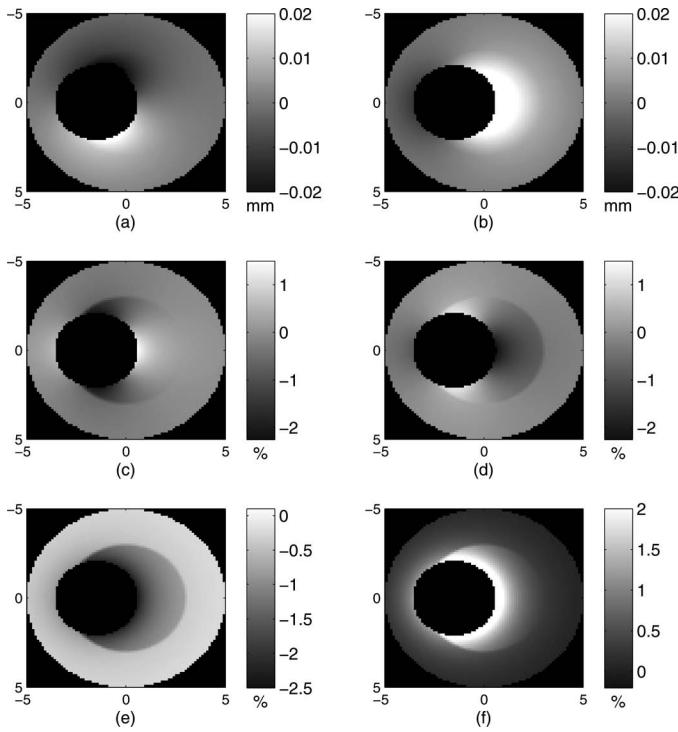


Fig. 9. The spatial variation of displacement and strain within a heterogeneous vessel, which was computed using the finite element method: (a) and (b) axial and lateral displacements, (c) and (d) axial and lateral strains, (e) and (f) radial and circumferential strain.

Transforming axial and lateral strain elastograms to the vessel coordinate system should improve the clinical use of NIVE. Coordinate transformation is relatively easy in cases in which accurate axial and lateral displacement estimates are available. Because ultrasound can only measure the axial component accurately, computing radial and strain elastograms via coordinate transformation has not been a viable approach. Figs. 5(a) and 5(b) demonstrate that sparse array systems can produce high-quality axial and lateral strain elastograms, which is consistent with results that we have reported in a previous study [24]. More specifically, we have demonstrated [24] that by using a synthetic-aperture ultrasound imaging system we could reconstruct RF echo frames with high lateral sampling frequency (50 lines/mm) and narrow lateral beam width (0.2 mm) that was required to produce accurate axial and lateral displacement estimates.

In this paper, we demonstrated that transforming normal and shear strain elastograms to the vessel coordinate system provides good radial and circumferential strain elastograms. Radial and circumferential strains were greatest on the inner lumen, but they decayed rapidly with increasing radial distance. This radial strain decay was consistent with theoretical predictions, and with those observed by other investigators [11], [39], [12]. The circumferential strain decay also agreed with theoretical predictions. To the best of our knowledge, this is the first reported study to demonstrate that an SA ultrasound

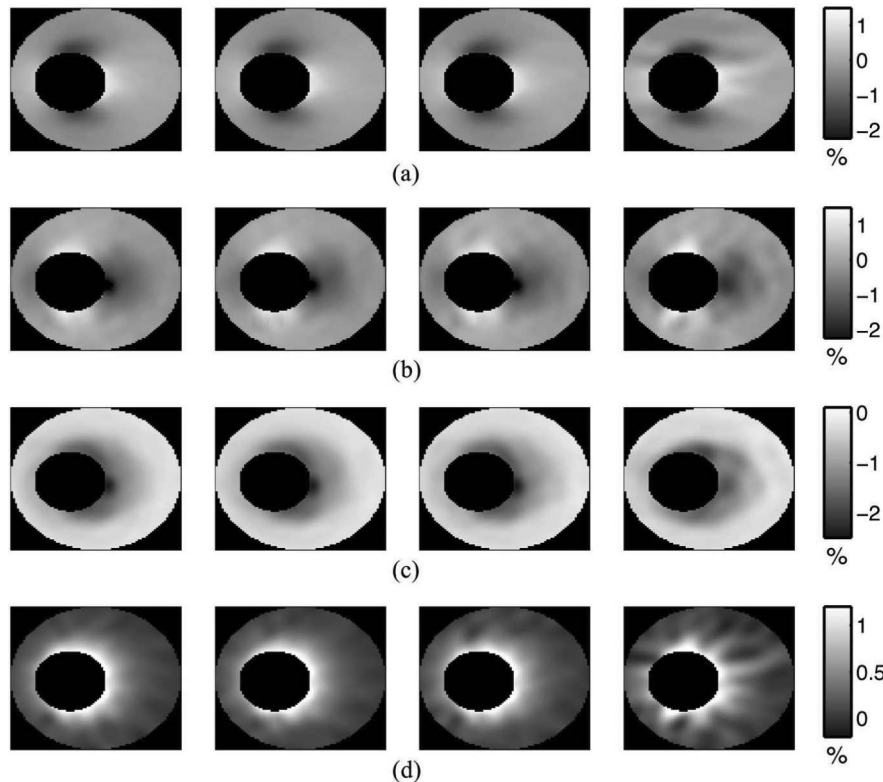


Fig. 10. Heterogeneous elastograms computed from simulated RF echo frames for transducer arrays with (left to right) 128, 32, 8, and 2 active transmission elements: (a) axial and (b) lateral strain elastograms, (c) radial and (d) circumferential strain elastograms. The marked ROIs denote the areas over which CNRe values reported in Fig. 11 were computed.

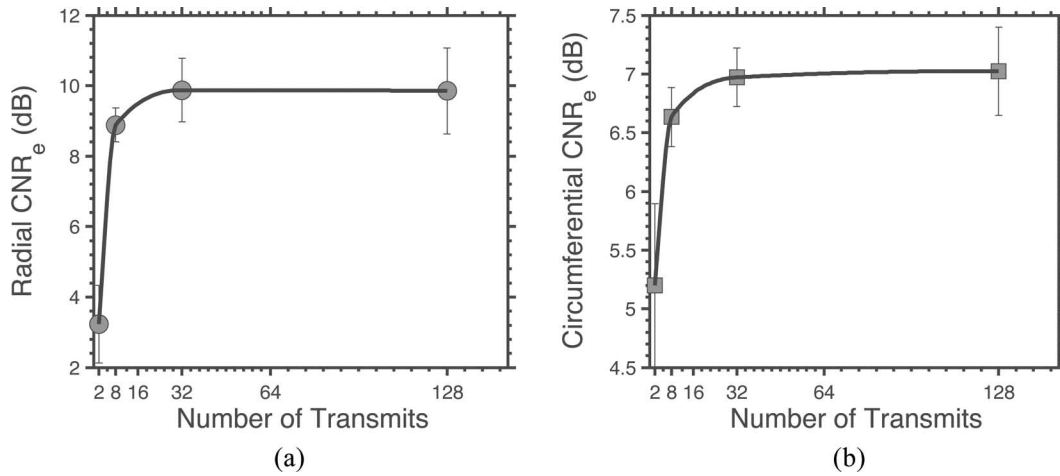


Fig. 11. Elastographic contrast-to-noise ratio (CNRe) plotted as function of number of active transmission elements. Showing the CNRe computed from (a) radial and (b) circumferential strain elastograms shown in Fig. 10.

elastography system could visualize circumferential strain decay with good spatial and contrast resolution.

Fig. 6 demonstrates that the mean radial and circumferential strains were independent of sparsity, but that the measured noise increased with sparsity; and that the noise incurred in the strain elastograms was dependent on radial distance. The noise observed in Fig. 6 represents a combination of strain dependent decorrelation noise [40] and changes in the PSF incurred when the number of transmission elements in the transducer array was varied. Fig. 8 demonstrates that the axial and lateral profiles of the PSF consisted of a main lobe and side-lobes. The main lobe determined the bias incurred when measuring axial and lateral displacements, whereas the side-lobes influenced the uncertainty incurred when measuring displacement—if significant, they could produce erroneous displacement estimates [18].

The number of active transmission elements did not affect the axial profile of the point spread functions, ex-

cept when transmission was performed with two active elements—a prominent main lobe and weak side-lobes were apparent. The axial profile of the PSF broadened when transmission was performed with two active elements because the waves emanating from the elements (one located at each end of the transducers) did not have sufficient energy to produce constructive interference. We estimated that the bias incurred when measuring radial displacements was between 1 and 3%, which was smaller than that incurred when the Von Mises parameter was interpreted as radial strain [11], and was on par with that achieved using compounding methods [39].

Fig. 8(b) demonstrates that although the main lobes of the lateral profiles of the PSF were similar, the side-lobe levels increased rapidly as the number of transmission elements was reduced. These results predict that, except for the cases in which imaging was performed with two active transmission elements, the mean circumferential strain estimated with different numbers of active transmission ele-

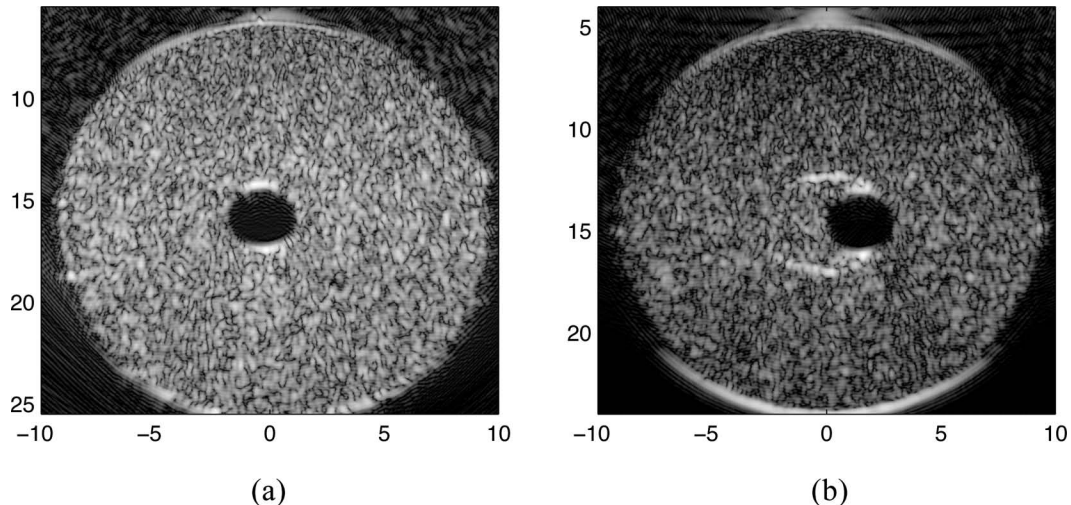


Fig. 12. Sonograms obtained from (a) homogeneous and (b) eccentric heterogeneous vessel phantoms using a 128-element synthetic-aperture ultrasound imaging system.

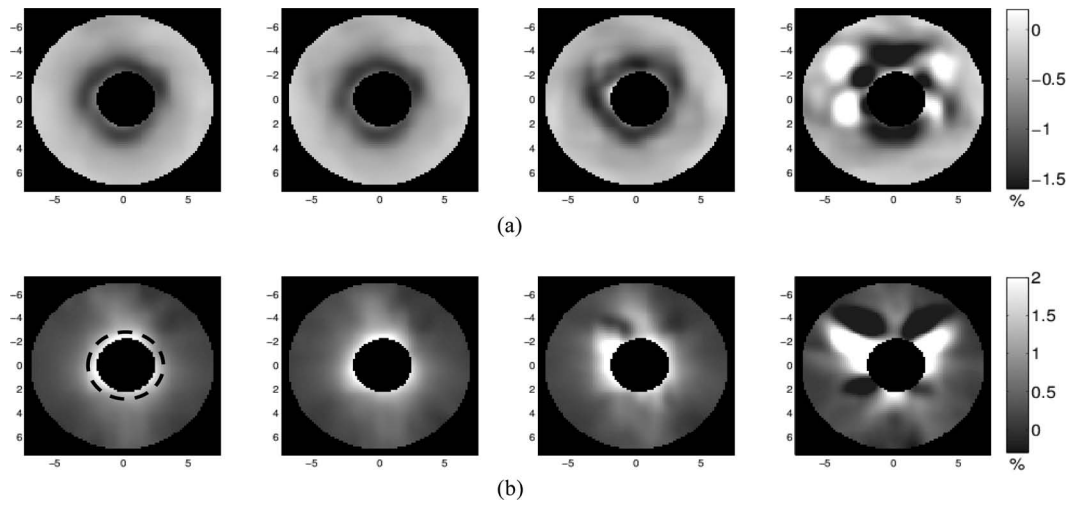


Fig. 13. (a) Radial and (b) circumferential strain elastograms obtained from a homogeneous vessel phantom with a 5-MHz linear transducer array that had 128, 32, 8, and 2 active transmission elements (left to right). The marked annulus denotes the area over which SNRe values reported in Fig. 15 were computed.

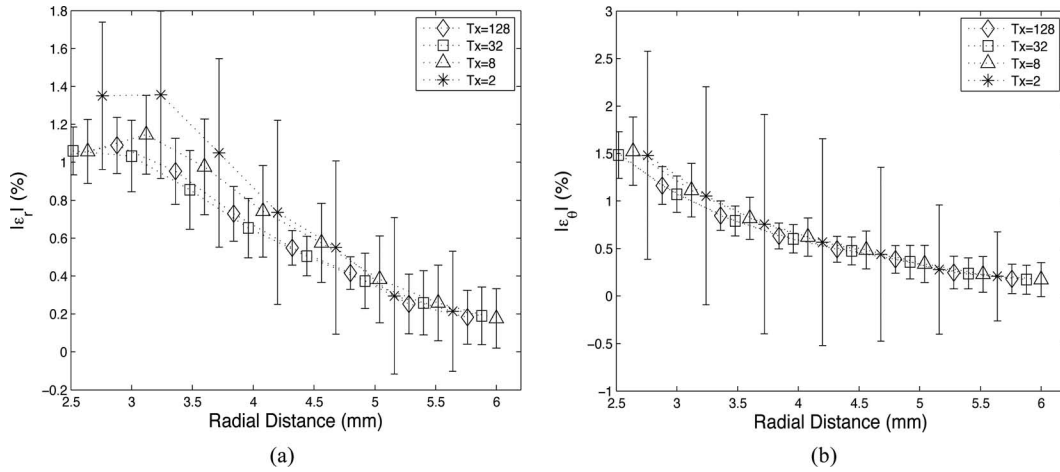


Fig. 14. (a) Radial and (b) circumferential strain profiles computed from the strain elastograms shown in Fig. 13.

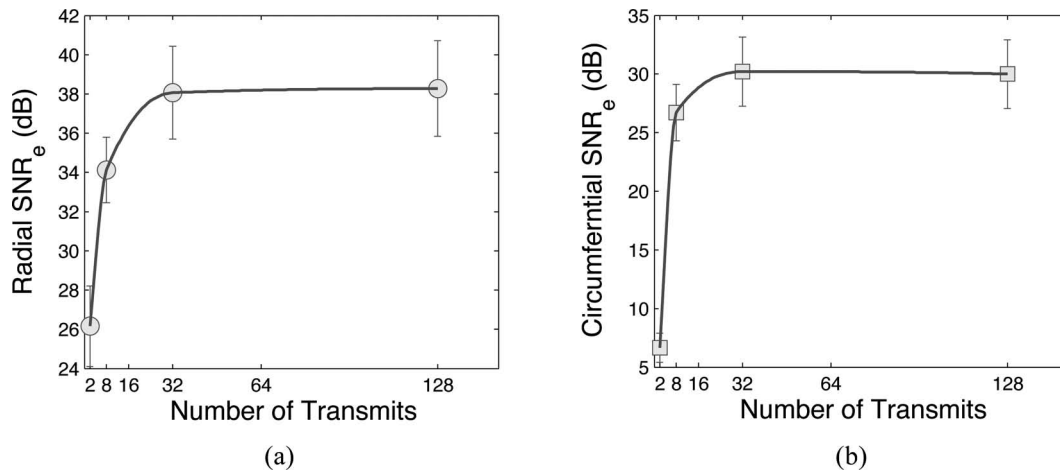


Fig. 15. The elastographic signal-to-noise ratio (SNRe) computed from (a) radial and (b) circumferential strain elastograms shown in Fig. 13.

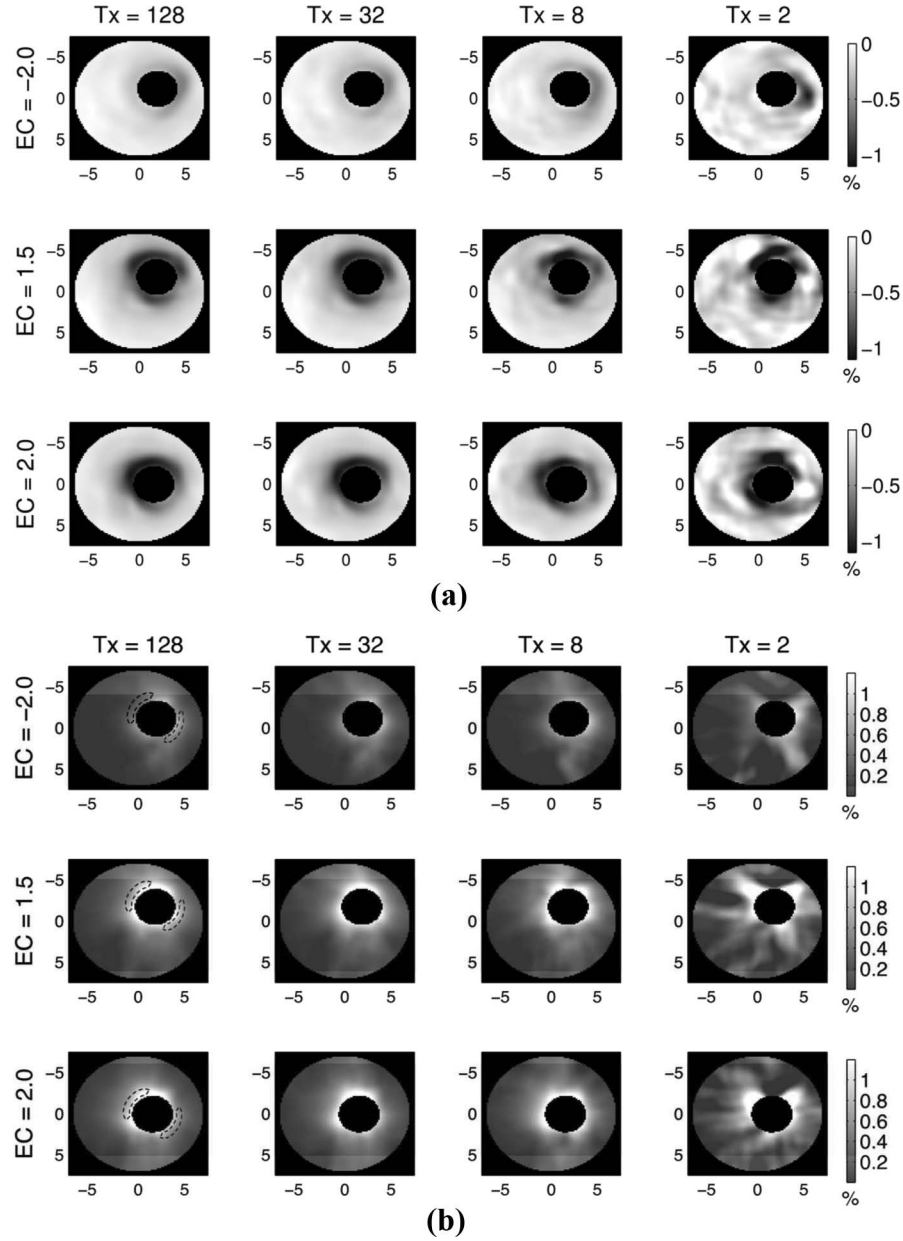


Fig. 16. (a) Circumferential strain elastograms obtained from heterogeneous vessel phantoms using a 5-MHz 128-element linear transducer array with (left to right) 128, 32, 8, and 2 active transmission elements. The marked ROIs denote the areas over which the elastographic contrast-to-noise ratio (CNRe) values reported in Fig. 17 were computed. (b) Radial strain elastograms obtained from heterogeneous vessel phantoms using a 5-MHz 128-element linear transducer array with (left to right) 128, 32, 8, and 2 active transmission elements. The marked ROIs denote the areas over which the CNRe values reported in Fig. 17 were computed.

ments (sparsity) should be similar to each other, but the variance should increase noticeably, which is consistent with the results shown in Fig. 7.

Reducing the number of transmission elements had two primary effects: 1) it broadened the PSF and increased

the lateral side-lobes, and 2) it reduces the power of the transmitted signal (this effect was not assessed in this study). Nevertheless, the side-lobe levels were sufficiently low, and there was enough power to produce good strain elastograms with eight active transmission elements (i.e.,

TABLE IV. THE ROOT MEAN SQUARE ERRORS (RMSEs) COMPUTED FROM HETEROGENEOUS DISPLACEMENT [AXIAL (DZ) AND LATERAL (DX)] AND STRAIN ELASTOGRAMS [RADIAL (ϵ_{RR}) AND CIRCUMFERENTIAL ($\epsilon_{\theta\theta}$)] OBTAINED WITH VARYING NUMBER OF ACTIVE TRANSMISSION ELEMENTS (Tx).

Tx	128	32	8	2
dz (μm)	0.720 ± 0.029	0.721 ± 0.035	0.739 ± 0.029	0.129 ± 0.037
dx (μm)	0.970 ± 0.156	0.980 ± 0.153	0.991 ± 0.155	0.114 ± 0.133
ϵ_{rr} (%)	0.184 ± 0.005	0.187 ± 0.003	0.198 ± 0.004	0.218 ± 0.003
$\epsilon_{\theta\theta}$ (%)	0.081 ± 0.005	0.082 ± 0.005	0.087 ± 0.004	0.146 ± 0.005

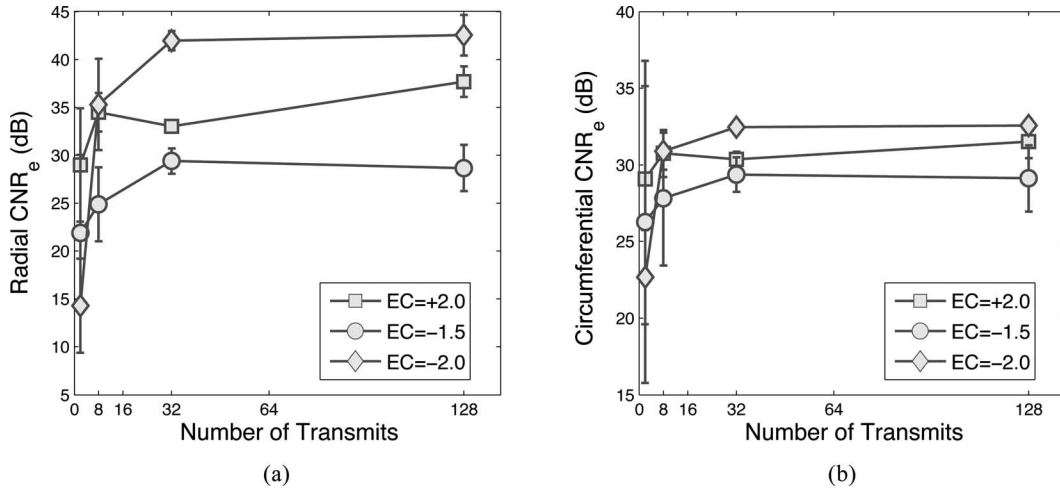


Fig. 17. The elastographic contrast-to-noise ratio (CNR_e) computed over the regions of interest defined in Fig. 16.

elastograms with SNR_e of 34 and 28 dB when measuring radial and circumferential strain, respectively).

Figs. 13 and 16 corroborated the predictions of the simulation. More specifically, our experimental results demonstrate that a SA elastographic system can visualize the radial and circumferential strain distribution within vessel phantoms, with excellent spatial and contrast resolution. Fig. 15 demonstrates that SNR_e values measured from homogeneous vessel phantoms were slightly lower than those predicted by the simulation study (i.e., SNR_e values of 21 and 11 dB were achieved when measuring radial and circumferential strain, respectively). Fig. 13 also demonstrates that radial and circumferential strain decays observed in the simulation study were also apparent in the phantom study. As in the simulation study, the mean radial and circumferential strain recovered from the phantoms were not affected by sparsity, with the exception of the sparsest array. However, the variance incurred in lateral displacement estimates increased with sparsity. The quality of the experimentally acquired radial strain elastograms would appear to be better than those reported by other group [11], [39], [12]. Furthermore, our circumferential strain elastograms appeared to be visually better than those reported in [39], [17]. The quality of circumferential strain elastograms obtained from the heterogeneous vessel phantom was worse than that observed in the simulation or the homogeneous phantom study. The most likely source of this discrepancy is the heterogeneous phantoms used in this study—creating stable heterogeneous vessel phantoms from gelatin can be challenging. To further investigate this discrepancy, we plan to conduct studies with cryogel phantoms. Fig. 17 demonstrates that radial and circumferential strain elastograms can visualize eccentric plaques with high contrast-to-noise ratio (between 10 and 40 dB) when the center of the lumen is known.

A limitation of this study was that all measurements were performed under quasi-static measurement conditions, rather than true physiological conditions. Therefore, we plan to conduct phantom studies using a pulsatile pressurization system similar to that described in [41].

Another limitation of the study was the boundary conditions used in the finite element models. More specifically, all nodes on the boundary were constrained from moving in both coordinate directions, which restricted the magnitude of the in-plane motion—much smaller than which would occur in practice. In future studies, we plan to resolve this issue by embedding the simulated artery in a softer material or coupling the boundary element method to the FEM.

In this study, we used a transmission frequency of 5 MHz, the highest allowable frequency that could be used with the L14-5/38 linear transducer array in an SA elastography system. A prerequisite to SA imaging is that an omnidirectional acoustic field must be emitted from each element in the array. The directivity function D of an element of size a is given by $D(\theta) = |\sin(\nu)/\nu|$, where $\nu = \lambda/a\sin(\theta)$ and θ is the direction of the field [42]. This requirement is not met when the size of the element is much larger than the transmitted wavelength—which was the case when we operated the L14-5/38 linear transducer at high transmission frequencies (>5 MHz).

Consequently, we are currently studying the performance of the synthetic aperture ultrasound elastographic system with different transmission frequencies and transducer designs. The results of this investigation will be reported in a future communication. The main limitation of using a sparse array system in the clinical setting is that it may not have sufficient transmit power to produce useful elastograms. Therefore, we plan to develop new strategies to cope with this potential problem. These include encoding the ultrasound signal or employing sub-aperture transmits. Additionally, we plan to evaluate the performance of the prototype system with excised tissues and volunteers.

V. CONCLUSIONS

We assessed the feasibility of using a synthetic-aperture ultrasound elastography system to visualize the radial and circumferential strain distribution within the carotid ar-

tery by conducting experiments on simulated and physical vessel phantoms. We demonstrated that an SA ultrasound imaging system can produce high-precision axial and lateral displacement estimates when transformed to the vessel coordinate system; these estimates will produce useful radial and circumferential strain elastograms. We also demonstrated that SA imaging with sparse arrays that contained as few as eight active transmission elements can produce high-quality strain elastograms that can be used to effectively characterize the arterial wall. The results of this work were sufficiently encouraging to warrant further studies into the role that SA ultrasound elastograms may play in cardiovascular imaging.

ACKNOWLEDGMENTS

We thank Dr. M. Karaman and Dr. M. Richards for their help.

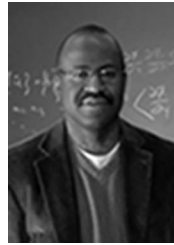
REFERENCES

- [1] J. Lloyd, "Heart disease and stroke statistics—2009 update: A report from the American Heart Association statistics committee and stroke statistics subcommittee," *Circulation*, vol. 122, no. 1, pp. E11–E11, 2010.
- [2] J. Blacher, B. Pannier, A. P. Guerin, S. J. Marchais, M. E. Safar, and G. M. London, "Carotid arterial stiffness as a predictor of cardiovascular and all-cause mortality in end-stage renal disease," *Hypertension*, vol. 32, no. 3, pp. 570–574, 1998.
- [3] Z. A. Fayad and V. Fuster, "Clinical imaging of the high-risk or vulnerable atherosclerotic plaque," *Circ. Res.*, vol. 89, no. 4, pp. 305–316, 2001.
- [4] J. A. Schaar, F. Mastik, E. Regar, C. A. den Uil, F. J. Gijzen, J. J. Wentzel, P. W. Serruys, and A. F. W. van der Steen, "Current diagnostic modalities for vulnerable plaque detection," *Curr. Pharm. Des.*, vol. 13, no. 10, pp. 995–1001, 2007.
- [5] K. Nieman, F. Cademartiri, R. Raaijmakers, P. Pattynama, and P. de Feyter, "Noninvasive angiographic evaluation of coronary stents with multi-slice spiral computed tomography," *Herz*, vol. 28, no. 2, pp. 136–142, 2003.
- [6] C. Yuan, K. Beach, L. Smith Jr., and T. Hatsukami, "Measurement of atherosclerotic carotid plaque size in vivo using high resolution magnetic resonance imaging," *Circulation*, vol. 98, no. 24, pp. 2666–2671, 1998.
- [7] M. L. Bots, A. W. Hoes, P. J. Koudstaal, A. Hofman, and D. E. Grobbee, "Common carotid intima-media thickness and risk of stroke and myocardial infarction—The Rotterdam study," *Circulation*, vol. 96, no. 5, pp. 1432–1437, 1997.
- [8] S. Ebrahim, O. Papacosta, P. Whincup, G. Wannamethee, M. Walker, A. N. Nicolaides, S. Dhanjil, M. Griffin, G. Belcaro, A. Rumley, and G. D. O. Lowe, "Carotid plaque, intima media thickness, cardiovascular risk factors, and prevalent cardiovascular disease in men and women—The British regional heart study," *Stroke*, vol. 30, no. 4, pp. 841–850, 1999.
- [9] M. W. Lorenz, H. S. Markus, M. L. Bots, M. Rosvall, and M. Sitzer, "Prediction of clinical cardiovascular events with carotid intima-media thickness—A systematic review and meta-analysis," *Circulation*, vol. 115, no. 4, pp. 459–467, 2007.
- [10] C. L. de Korte, M. J. Siervogel, F. Mastik, C. Strijder, J. A. Schaar, E. Velema, G. Pasterkamp, P. W. Serruys, and A. F. van der Steen, "Identification of atherosclerotic plaque components with intravascular ultrasound elastography in vivo: A Yucatan pig study," *Circulation*, vol. 105, no. 14, pp. 1627–1630, 2002.
- [11] R. L. Maurice, J. Ohayon, Y. Fretigny, M. Bertrand, G. Soulez, and G. Cloutier, "Noninvasive vascular elastography: Theoretical framework," *IEEE Trans. Med. Imaging*, vol. 23, no. 2, pp. 164–180, 2004.
- [12] H. Ribbers, R. G. P. Lopata, S. Holewijn, G. Pasterkamp, J. D. Blankensteijn, and C. L. de Korte, "Noninvasive two-dimensional strain imaging of arteries: Validation in phantoms and preliminary experience in carotid arteries in vivo," *Ultrasound Med. Biol.*, vol. 33, no. 4, pp. 530–540, 2007.
- [13] T. Zakaria, Z. Qin, and R. L. Maurice, "Optical-flow-based B-mode elastography: Application in the hypertensive rat carotid," *IEEE Trans. Med. Imaging*, vol. 29, no. 2, pp. 570–578, 2010.
- [14] C. Schmitt, G. Soulez, R. L. Maurice, M. F. Giroux, and G. Cloutier, "Noninvasive vascular elastography: Toward a complementary characterization tool of atherosclerosis in carotid arteries," *Ultrasound Med. Biol.*, vol. 33, no. 12, pp. 1841–1858, 2007.
- [15] R. Maurice, G. Soulez, M. Giroux, and G. Cloutier, "Noninvasive vascular elastography for carotid artery characterization on subjects without previous history of atherosclerosis," *Med. Phys.*, vol. 35, no. 8, pp. 3436–3443, 2008.
- [16] H. Hasegawa and H. Kanai, "Simultaneous imaging of artery-wall strain and blood flow by high frame rate acquisition of RF signals," *IEEE Trans. Ultrason. Ferroelectr. Freq. Control*, vol. 55, no. 12, pp. 2626–2639, 2008.
- [17] H. H. G. Hansen, R. G. P. Lopata, and C. L. de Korte, "Noninvasive carotid strain imaging using angular compounding at large beam steered angles: Validation in vessel phantoms," *IEEE Trans. Med. Imaging*, vol. 28, no. 6, pp. 872–880, 2009.
- [18] M. Lubinski, S. Emelianov, and M. O'Donnell, "Speckle tracking methods for ultrasonic elasticity imaging using short-time correlation," *IEEE Trans. Ultrason. Ferroelectr. Freq. Control*, vol. 46, no. 1, pp. 82–96, 1999.
- [19] M. E. Anderson, "Multi-dimensional velocity estimation with ultrasound using spatial quadrature," *IEEE Trans. Ultrason. Ferroelectr. Freq. Control*, vol. 45, no. 3, pp. 852–861, 1998.
- [20] A. Basarab, P. Gueth, H. Liebgott, and P. Delachartre, "Phase-based block matching applied to motion estimation with unconventional beamforming strategies," *IEEE Trans. Ultrason. Ferroelectr. Freq. Control*, vol. 56, no. 5, pp. 945–957, 2009.
- [21] P. Gueth, A. Basarab, H. Liebgott, and P. Delachartre, "Beamforming techniques for motion estimation in ultrasound elastography," in *IEEE Ultrasonics Symp.*, pp. 1953–1956, 2007.
- [22] C. Sumi, "Displacement vector measurement using instantaneous ultrasound signal phase—Multidimensional autocorrelation and Doppler methods," *IEEE Trans. Ultrason. Ferroelectr. Freq. Control*, vol. 55, no. 1, pp. 24–43, 2008.
- [23] E. E. Konofagou and J. Ophir, "A new elastographic method for estimation and imaging of lateral displacements, lateral strains, corrected axial strains and Poisson's ratio in tissues," *Ultrasound Med. Biol.*, vol. 24, no. 8, pp. 1183–1199, 1997.
- [24] S. Korukonda and M. M. Doyley, "Axial and lateral strain estimation using a synthetic aperture elastographic imaging system," *Ultrasound Med. Biol.*, vol. 37, no. 11, pp. 1893–1908, 2011.
- [25] R. Y. Chiao and L. J. Thomas, "Analytic evaluation of sampled aperture ultrasonic-imaging techniques for NDE," *IEEE Trans. Ultrason. Ferroelectr. Freq. Control*, vol. 41, no. 4, pp. 484–493, 1994.
- [26] C. R. Cooley and B. S. Robinson, "Synthetic focus imaging using partial datasets," in *IEEE Ultrasonics Symp.*, 1994., vol. 3, pp. 1539–1542.
- [27] G. R. Lockwood and F. S. Foster, "Design of sparse array imaging systems," in *IEEE Ultrasonics Symp.*, 1995, vol. 2, pp. 1237–1243.
- [28] J. A. Jensen and N. B. Svendsen, "Calculation of pressure fields from arbitrarily shaped, apodized, and excited ultrasound transducers," *IEEE Trans. Ultrason. Ferroelectr. Freq. Control*, vol. 39, no. 2, pp. 262–267, 1992.
- [29] R. F. Wagner, S. Smith, J. M. Sandrik, and H. Lopez, "Statistics of speckle in ultrasound B-scans," *IEEE Trans. Sonics Ultrason.*, vol. 30, no. 3, pp. 156–163, 1983.
- [30] C. de Korte, E. Céspedes, A. van der Steen, and C. Lancée, "Intravascular elasticity imaging using ultrasound: Feasibility studies in phantoms," *Ultrasound Med. Biol.*, vol. 23, no. 5, pp. 735–746, 1997.
- [31] R. Y. Chiao and L. J. Thomas, "Aperture formation on reduced-channel arrays using the transmit-receive apodization matrix," in *IEEE Ultrasonics Symp.*, 1996, pp. 1567–1571.
- [32] M. M. Doyley, J. C. Bamber, F. Fuechsel, and N. L. Bush, "A free-hand elastographic imaging approach for clinical breast imaging: System development and performance evaluation," *Ultrasound Med. Biol.*, vol. 27, no. 10, pp. 1347–1357, 2001.
- [33] R. Cook, D. Malkus, M. Plesha, and R. Witt, *Concepts and Applications of Finite Element Analysis*. New York, NY: Wiley, 2007.

- [34] P. Chaturvedi, M. Insana, and T. Hall, "2-D companding for noise reduction in strain imaging," *IEEE Trans. Ultrason. Ferroelectr. Freq. Control*, vol. 45, no. 1, pp. 179–191, 1998.
- [35] C. L. de Korte, E. I. Cespedes, A. F. van der Steen, G. Pasterkamp, and N. Bom, "Intravascular ultrasound elastography: Assessment and imaging of elastic properties of diseased arteries and vulnerable plaque," *Eur. J. Ultrasound*, vol. 7, no. 3, pp. 219–224, 1998.
- [36] C. L. de Korte and A. F. van der Steen, "Intravascular ultrasound elastography: An overview," *Ultrasonics*, vol. 40, no. 1–8, pp. 859–865, 2002.
- [37] C. L. de Korte, A. F. van der Steen, E. I. Cespedes, and G. Pasterkamp, "Intravascular ultrasound elastography in human arteries: Initial experience in vitro," *Ultrasound Med. Biol.*, vol. 24, no. 3, pp. 401–408, 1998.
- [38] C. L. de Korte, A. F. van der Steen, E. I. Cepedes, G. Pasterkamp, S. G. Carlier, F. Mastik, A. H. Schoneveld, P. W. Serruys, and N. Bom, "Characterization of plaque components and vulnerability with intravascular ultrasound elastography," *Phys. Med. Biol.*, vol. 45, no. 6, pp. 1465–1475, 2000.
- [39] H. H. G. Hansen, R. G. P. Lopata, T. Idzenga, and C. L. de Korte, "An angular compounding technique using displacement projection for noninvasive ultrasound strain imaging of vessel cross-sections," *Ultrasound Med. Biol.*, vol. 36, no. 11, pp. 1947–1956, 2010.
- [40] T. Varghese and J. Ophir, "A theoretical framework for performance characterization of elastography: The strain filter," *IEEE Trans. Ultrason. Ferroelectr. Freq. Control*, vol. 44, no. 1, pp. 164–172, 1997.
- [41] M. M. Doyley, F. Mastik, C. L. De Korte, S. G. Carlier, E. I. Cespedes, P. W. Serruys, N. Bom, and A. F. W. Van der Steen, "Advancing intravascular ultrasonic palpation toward clinical applications," *Ultrasound Med. Biol.*, vol. 27, no. 11, pp. 1471–1480, 2001.
- [42] L. Kinsler, A. Frey, A. Coppens, and J. Sanders, *Fundamentals of Acoustics*, 4th ed., vol. 1, New York, NY: Wiley-VCH, 1999.



Sanghamithra Korukonda received her dual degree in electrical engineering with a specialization in communication and signal processing from the Indian Institute of Technology, Bombay, in 2002. From 2003 to 2007, she was a research engineer at GE Research, Bangalore, working on non-invasive imaging for industrial applications. She graduated from the University of Rochester, NY, in 2012 with a Ph.D. degree in biomedical ultrasound. Her research interests include ultrasound beamforming, synthetic aperture imaging, and quasi-static elastography.



Marvin M. Doyley received his Ph.D degree in biophysics from the University of London in 2000. His dissertation topic was an investigation into methods for improving the clinical usefulness of elasticity imaging. From 2000 to 2001, he was with the experimental echocardiography department at the Thorax Center in the Netherlands. From 2001 to 2008, he was with the Thayer School of Engineering at Dartmouth College as a research faculty member. In 2008, he joined the faculty of the Department of Electrical and Engineering at the University of Rochester. His research interests include cardiovascular, molecular imaging, elastography, harmonic, and model-based imaging.